

OPEN ACCESS

Preparation of Low Surface Area Si-Alloy Anodes for Li-Ion Cells by Ball Milling

To cite this article: Simeng Cao *et al* 2022 *J. Electrochem. Soc.* **169** 060540

View the [article online](#) for updates and enhancements.



ECS Membership = Connection

ECS membership connects you to the electrochemical community:

- Facilitate your research and discovery through ECS meetings which convene scientists from around the world;
- Access professional support through your lifetime career;
- Open up mentorship opportunities across the stages of your career;
- Build relationships that nurture partnership, teamwork—and success!



Join ECS!

Visit electrochem.org/join





Preparation of Low Surface Area Si-Alloy Anodes for Li-Ion Cells by Ball Milling

Simeng Cao,¹ Mohammad H. Tahmasebi,^{1,*}  Shayne Gracious,¹ J. Craig Bennett,² and M. N. Obrovac^{1,3,*} 

¹Department of Chemistry, Dalhousie University, Halifax, Nova Scotia B3H 4R2, Canada

²Department of Physics, Acadia University, Wolfville, Nova Scotia B4P 2R6, Canada

³Department of Physics and Atmospheric Science, Dalhousie University, Halifax, Nova Scotia B3H 4R2, Canada

A new and simple 2-step milling technique is utilized to produce Si–Ti–N alloys with significantly reduced surface area compared to conventional ball milling, while still attaining a full amorphous active Si phase. Surface area reductions of up to 100% were obtained by this method. Surprisingly, this did not result in significant differences in cycling stability compared to conventionally ball milled high surface area alloy materials. This is likely because cycling caused severe fracturing of the alloy surfaces, resulting in a high surface area, regardless of the initial surface area of the alloy. This suggests that, unlike other anode materials such as graphite, reducing the initial surface area of Si alloys does not translate into reduced electrolyte reactivity.

© 2022 The Author(s). Published on behalf of The Electrochemical Society by IOP Publishing Limited. This is an open access article distributed under the terms of the Creative Commons Attribution 4.0 License (CC BY, <http://creativecommons.org/licenses/by/4.0/>), which permits unrestricted reuse of the work in any medium, provided the original work is properly cited. [DOI: 10.1149/1945-7111/ac797e]



Manuscript submitted April 8, 2022; revised manuscript received June 8, 2022. Published June 27, 2022.

Supplementary material for this article is available [online](#)

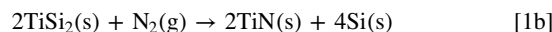
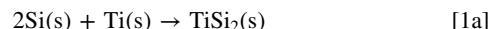
Si alloys are an attractive anode material for Li-ion batteries.^{1–3} Such alloys need a high silicon content (typically greater than 50 atomic percent) for lithium battery applications, so that they can have high lithium storage capacity. Additionally, Si-based anodes should be nanostructured or amorphous to reduce particle fracturing and suppress $\text{Li}_{15}\text{Si}_4$ formation during lithiation, that has been associated with high electrolyte reactivity, alloy particle fracture, and poor cycling characteristics.^{4,5} A low-cost method of making Si-alloys is by ball milling. Since high Si content alloys are brittle, ball milling typically results in the formation of submicron Si-alloy particles with high surface area.^{6,7} It is well known that high surface area is detrimental for anode materials because higher surface areas result in greater electrolyte reactivity. This leads to poor cell performance due to the consumption of Li ions in electrolyte decomposition reactions and high polarization due to electrolyte depletion and excessive solid electrolyte interphase (SEI) formation.^{8–10} It would therefore be advantageous if the surface area of ball milled Si-alloys could be reduced.

Si–M alloys (M = a transition metal) contain a ductile M-component. To see how the surface area of ball milled Si–M alloys might be reduced, it is instructive to review the mechanism by which nanostructured or amorphous alloys can be formed from ductile precursor metals during ball milling. One such mechanism has been described by Lee et al. for Ni–Ta alloys.¹¹ In Fig. 1 the observations by Lee et al. have been rendered as trendlines to show approximate trends in reaction extent, product particle size, product surface area, and product grain size during ball milling. During ball milling, powder particles that are positioned between colliding balls are repeatedly cold welded, fractured, and rewelded.¹² If the precursor powders contain at least one ductile material, then powder particles tend to weld together to form large particles in the early stage of milling (A). With longer milling times, ball collisions cause continuous plastic deformation of the powder particles, resulting in work hardening and fracture (B). The tendency to fracture predominates over cold welding, and particle and grain sizes are reduced at this stage of milling. Finally (C), a balance between cold welding and fracturing can be reached and grain and particle sizes reach a steady state. During this process, chemical reactions between the precursors occur. In Fig. 1 the reaction extent has been drawn to roughly follow the observations by Lee et al. for the Ni–Ta

system, in which the completion of the reaction between Ni and Ta occurred sometime during region C in Fig. 1. However, the region in the diagram at which chemical reactions between reactant particles reach completion likely depends upon the reactants involved.

Figure 1 clearly illustrates the dilemmas in making low surface area Si–M alloys by ball milling Si and M powders. Even though large particle sizes and low surface area alloys might be attained by stopping the ball milling process at the end of Region A, such an alloy would have large grain sizes, be inhomogeneous, and any milling reactions may not be complete. During lithiation, such alloys would be susceptible to fracture along grain boundaries and the formation of $\text{Li}_{15}\text{Si}_4$ by large Si crystallites; both processes being generally detrimental for cycling.¹³ On the other hand, if small grain sizes or full amorphization is achieved to enable good electrochemical cycling characteristics, this requires ball milling for sufficient time until region C is encountered, in which small particle sizes and high surface areas result. This latter case typically describes how most Si–M alloys reported in the literature are prepared. However, the high surface areas of such materials would tend to accelerate parasitic surface reactions between the active alloy particles and the electrolyte during cell cycling.

The goal of the present study was to make ball milled Si-based alloys that combine the properties having an amorphous or nanocrystalline grain structure with low particle surface area. The Si–TiN alloy composition was identified previously as being promising for Li-ion batteries because of its good cycling characteristics and high thermal stability (making it amenable towards carbon coating by chemical vapor deposition).^{5,6,14} Si–TiN alloys may be formed by reactive gas ball milling of Si and Ti powders in $\text{N}_2(\text{g})$. Under these conditions, Si–TiN alloys are formed according to 2 consecutive reactions:^{5,6,14}



where the metastable C49 TiSi_2 phase is formed in Eq. 1a and where Eq. 1b does not proceed until Eq. 1a has completed. It has not been established why this peculiar 2-stage consecutive reaction mechanism is followed. In order to make low surface area Si–TiN alloys, the particle size, grain size, and reaction extent of Si and Ti powders were studied during milling in N_2 gas.

Here, Si–Ti–N alloys were synthesized by ball milling and the alloy surface area, particle morphology, grain morphology and phase

*Electrochemical Society Member.

^zE-mail: mnobrovac@dal.ca

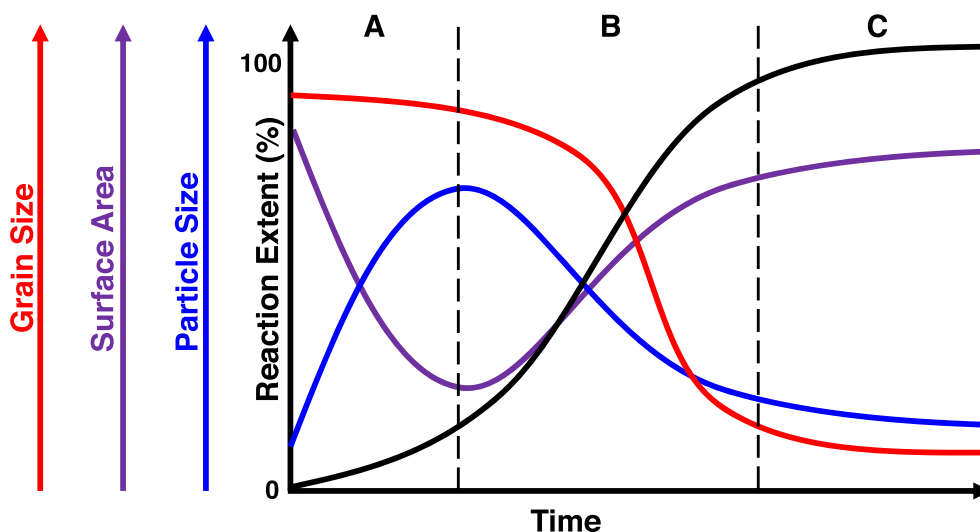


Figure 1. Illustration of proposed trends in reaction extent, product particle size, product surface area, and product grain size during the ball milling of metal precursors to form alloys.

composition were followed as a function of milling time, to understand how these properties change. This allowed a better understanding of the 2-stage reaction shown as Eqs. 1a and 1b. Using these trends, a unique 2-step milling protocol was developed to produce Si–Ti–N alloys that combine an amorphous/nanocrystalline grain structure with low surface area. Electrochemical performance of the resulting Si–Ti–N samples was then investigated. It is also shown that the 2-step milling strategy can also be used to significantly reduce the surface area of other compositions, such as SiO.

Experimental

In order to study particle size evolution during milling, Si powder (Sigma-Aldrich, 325 mesh, 99%) and ductile Ti powder (Alfa Aesar, 325 mesh, 99%) were mechanical milled in Ar or N₂ (g) for different milling times. The Si and Ti powders (the total volume: 0.5 ml based on true powder density) with certain stoichiometric ratios (Si₈₅Ti₁₅, Si₇₀Ti₃₀ or Si₆₀Ti₄₀) were loaded into a ball milling vial (SPEX CertiPrep, 65 ml, hardened steel) with 180 g stainless steel balls (d = 0.125 inch). The milling conditions used here were optimized in previous work.¹⁵ For Ar milling, the milling vials were flushed with Ar, and sealed in an Ar-filled glovebox. Then, the milling vials were placed in a high energy ball mill (Spex Mixer Mill Model 8000D, Spex CertiPrep, Metuchen, NJ) for sample preparation. In the case of N₂ (g) milling, the milling vials were closed in an Ar-filled glovebox with the o-ring seals removed. This allowed gas to flow in and out of the vials during the milling process. The ball mill used for N₂ (g) milling was modified by enclosing the entire mill in a sealed outer chamber equipped with a gas inlet and outlet. The gas outlet was connected to an oil bubbler. The gas inlet was connected to a compressed nitrogen cylinder via a gas regulator and flowmeter. The milling vial was placed in the clamp of the specially designed ball mill, the outer chamber was sealed and N₂ (g) was purged through the chamber in order that the air inside was displaced. The mill was then operated under flowing N₂ (g) with a constant pressure of about 1 bar. After milling, all the samples prepared in this study were collected through another 5 min mill with ethanol, and more details about sample collection can be found in Ref. 5.

To prepare Si_{62.5}Ti_{26.8}N_{10.7} via a 2-step milling method, 0.84561 g of Si and 0.25433 g of Ti powders were milled in N₂ (g) for 16 h, to give a Si₈₅(TiN)₁₅ alloy. The sample was not collected after this milling step. In the second milling step, 0.36334 g of Ti powder was added into the mill vial with the milled sample

(corresponding to a final alloy composition of Si_{62.5}Ti_{26.8}N_{10.7}, which has a Si/Ti molar ratio of 70/30), and the mixture was further milled in Ar for different times (0–180 min).

X-ray diffraction (XRD) patterns were measured using a Rigaku Ultima IV diffractometer with a Cu K α X-ray source, a graphite diffracted beam monochromator and a scintillation counter detector. Morphology of samples and electrode cross sections was characterized using a Schottky field emission scanning electron microscope (SEM, TESCAN MIRA 3 IMU). Secondary electron (SE) images for samples morphology were obtained at a 20 kV accelerating voltage. Backscattered electron (BSE) images of electrode cross sections were collected with an operating voltage of 5 kV. Specific surface area of samples was determined through a surface area analyzer (Micromeritics FlowSorb II 2300). True sample densities were measured with a helium pycnometer (AccuPyc II 1340, Micromeritics).

Electrode slurries were prepared by mixing sample, carbon black (Super C, Timcal), a 10 wt% aqueous solution of lithium polyacrylate (LiPAA), carbon nanotubes (CNTs), graphite (SFG6L, Timcal) with an alloy/carbon black/LiPAA/CNTs/SFG6L volume ratio of 70/5/25/-/-, 46/3.5/16.5/34/-, or 35/20/2.5/12.5/26 in distilled water. Isopropanol (10 wt% in the mixture of alloy, carbon black, LiPAA, and isopropanol) was added to the slurries as a wetting agent. The mixing was conducted using a planetary mill with 3 tungsten carbide balls (d = 0.4375 inch) at 100 rpm for 1 h. Then, the slurries were spread onto copper foil (Furukawa Electric, Japan) with a 0.004-inch gap steel coating bar and dried in air at 120 °C for 1 h.

Disk electrodes (d = 13 mm) with a typical electrode loading of about 2 mAh cm⁻² were cut with an electrode punch. The electrodes were dried under vacuum at 120 °C for 2 h without further air exposure before cell assembly. Each electrode was assembled into a 2325-type coin cell with two Celgard 2300 separators and a lithium metal foil (99.9%, Sigma-Aldrich) counter/reference electrode under Ar atmosphere. If not otherwise specified, electrolyte was a 1 M LiPF₆ ethylene carbonate (EC)/diethyl carbonate (DEC)/monofluoroethylene carbonate (FEC) (30/60/10 v/v/v, all from BASF) solution. An electrolyte without FEC was also used in some cases. The cells were galvanostatically cycled at 30.0 °C \pm 0.1 °C between 0.005 V and 0.9 V with a Neware test system. A C/10 rate and a C/5 rate were applied for the 1st cycle and for the following cycles, respectively. During the lithiation half cycle, a pseudo trickle discharge was used after 0.005 V was reached, as described in Ref. 5. To accurately determine C-rates, trial cells were cycled at a

C/10 rate based on their theoretical capacity (assuming that all the Si in the alloy was active with a capacity of 3578 mAh g^{-1}). In this way, actual capacity of each alloy can be obtained from these trial cells. These measured capacities were used for calculating the cell C-rates in the cycling test.

Results and Discussion

Si and Ti in 85/15, 70/30, and 60/40 atomic ratios were ball milled in $\text{N}_2(\text{g})$ for 30–960 min. XRD patterns of the resulting $\text{Si}_{85}\text{Ti}_{15}(\text{N}_2)$, $\text{Si}_{70}\text{Ti}_{30}(\text{N}_2)$, and $\text{Si}_{60}\text{Ti}_{40}(\text{N}_2)$ alloys are shown in Figs. 2a–2c. After 30 min of milling, only a reduction in grain size of the initial starting elemental powders is evident. After longer milling times, XRD peaks from the C49 TiSi_2 phase appear in the XRD patterns and after 960 min of milling time the XRD patterns consist of peaks due to amorphous/nanocrystalline Si and nanocrystalline TiN phases. A small peak due to Fe contamination from the milling media was additionally observed in the $\text{Si}_{60}\text{Ti}_{40}(\text{N}_2, 960 \text{ min})$ sample. This evolution of Si–Ti alloys during reactive ball milling in $\text{N}_2(\text{g})$ has been described previously.^{5,6} Briefly, during the formation of these alloys under these conditions, Si and Ti first react to form the C49 TiSi_2 phase, as observed by XRD. This phase then becomes consumed as the reaction proceeds, with the formation of TiN, as confirmed by selected area electron diffraction.⁵ No silicon nitride phases are formed during this process, as confirmed by the lack of Si_3N_4 peaks in XRD patterns and by XPS analysis.⁵ Compositional analysis shows that after the reaction is complete, nitrogen is incorporated in the alloy such that the N:Ti ratio is about 1:1, further confirming TiN formation with no other nitride phases formed.^{5,6} TEM studies of the $\text{Si}_{70}\text{Ti}_{30}(\text{N}_2)$ alloy formed after 960 min of milling have shown that this alloy consists of $\sim 10 \text{ nm}$ TiN nanocrystallites dispersed in an a-Si matrix. This suggests the following reaction path for the evolution of Si–Ti alloys during reactive ball milling in $\text{N}_2(\text{g})$. Initially, Si and Ti react to form the C49 TiSi_2 phase (0–90 min). The C49 TiSi_2 phase then reacts with $\text{N}_2(\text{g})$ to produce TiN and amorphous (a-Si) with continued milling.

To confirm this reaction path, the nitrogen and oxygen content of the $\text{Si}_{70}\text{Ti}_{30}(\text{N}_2)$ series of samples was analyzed by the Leco method. All samples were found to contain about 5–8 at% oxygen, due

partially to the ~ 8 at% oxygen impurity content of the starting Si powder.^{5,6} The evolution in the nitrogen content of the series of samples with milling time is shown in Fig. S1 (available online at stacks.iop.org/JES/169/060540/mmedia). Consistent with the XRD results, for samples milled less than 960 min, only a small amount of nitrogen (~ 5 at%) was detected during milling. After 960 min milling, the nitrogen content increased to 18 at%, corresponding to the observation of TiN formation by XRD. According to the nitrogen and oxygen analysis results, the final composition of the $\text{Si}_{85}\text{Ti}_{15}(\text{N}_2)$ and $\text{Si}_{70}\text{Ti}_{30}(\text{N}_2)$ samples after 960 min milling time were $\text{Si}_{67.6}\text{Ti}_{11.9}\text{N}_{15.0}\text{O}_{5.5}$ and $\text{Si}_{51.3}\text{Ti}_{22.0}\text{N}_{18.0}\text{O}_{8.5}$, respectively. Both samples containing Ti and N in a ratio close to the 1:1 ratio according to the above reaction model. However, the final nitrogen content of the $\text{Si}_{70}\text{Ti}_{30}(\text{N}_2)$ is slightly below this value. At a higher titanium content of $\text{Si}_{60}\text{Ti}_{40}(\text{N}_2)$, peaks due to unreacted Ti can be seen in the XRD pattern. This is likely due to the high ductility of the Ti phase, which may be impeding the ability of samples with high Ti content to react fully to form silicides and nitride phases during milling.

Figures 3a–3c show SEM SE images of the $\text{Si}_{85}\text{Ti}_{15}(\text{N}_2)$, $\text{Si}_{70}\text{Ti}_{30}(\text{N}_2)$, and $\text{Si}_{60}\text{Ti}_{40}(\text{N}_2)$ alloys, respectively, at different stages during the milling process. After about 30 min of milling, the $\text{Si}_{85}\text{Ti}_{15}(\text{N}_2)$ alloy comprises small ($\sim 0.5 \mu\text{m}$) particles that are either present as individual particles or aggregated into larger secondary particles that are up to about $4 \mu\text{m}$ in size. For samples with higher Ti content, the particle sizes become bigger ($\sim 2 \mu\text{m}$ for $\text{Si}_{70}\text{Ti}_{30}(\text{N}_2)$ and $\sim 3 \mu\text{m}$ for $\text{Si}_{60}\text{Ti}_{40}(\text{N}_2)$). According to the XRD patterns, these samples consist mainly of unreacted crystalline Si (x-Si) and Ti phases. Therefore, the larger sizes of the higher Ti-containing alloys are consistent with enhanced cold welding due to the presence of more Ti ductile phase.

After 60 min of milling, flakes are seen to form in the alloys. Very few and only small flakes can be seen in the $\text{Si}_{85}\text{Ti}_{15}(\text{N}_2)$ alloy. As the Ti content is increased the flakes become more numerous and larger (both in breadth and width). After about 75 min of milling the flakes reach their largest size and are largest ($\sim 0.5 \mu\text{m} \times 5 \mu\text{m}$) for $\text{Si}_{60}\text{Ti}_{40}(\text{N}_2)$, the most Ti-rich composition. This sample also contains very few small alloy particles. In contrast, the Ti-poor $\text{Si}_{85}\text{Ti}_{15}(\text{N}_2)$ alloy still contains many irregularly shaped

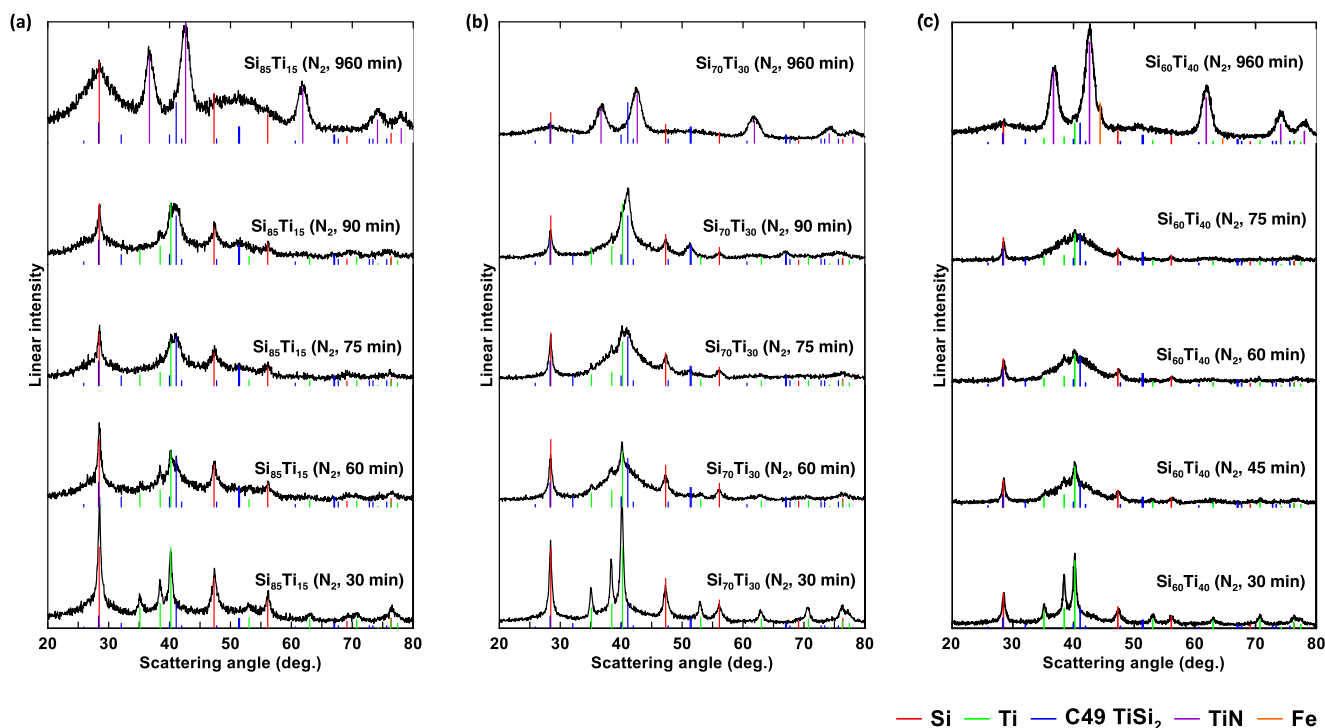


Figure 2. XRD patterns of (a) $\text{Si}_{85}\text{Ti}_{15}(\text{N}_2, 30\text{--}960 \text{ min})$, (b) $\text{Si}_{70}\text{Ti}_{30}(\text{N}_2, 30\text{--}960 \text{ min})$, and (c) $\text{Si}_{60}\text{Ti}_{40}(\text{N}_2, 30\text{--}960 \text{ min})$ samples.

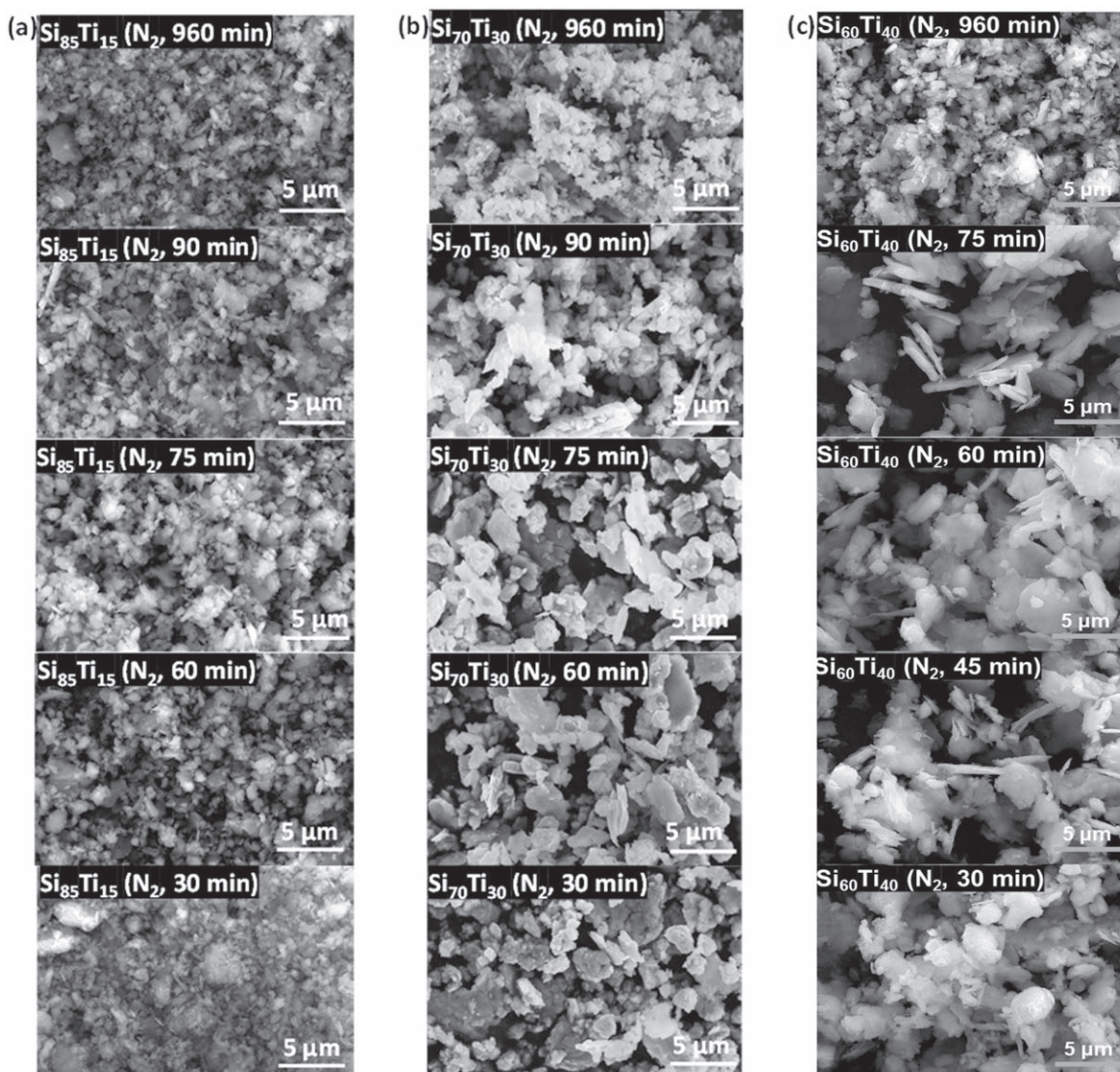


Figure 3. SEM SE images of (a) $\text{Si}_{85}\text{Ti}_{15}$ (N_2 , 30–960 min), (b) $\text{Si}_{70}\text{Ti}_{30}$ (N_2 , 30–960 min), and (c) $\text{Si}_{60}\text{Ti}_{40}$ (N_2 , 30–960 min) samples.

submicron particles. According to the XRD patterns shown in Fig. 2, the alloys consist mostly of α -Si, β -Si, TiSi_2 , and a small amount of Ti. Except for Ti, all these phases are brittle. Considering the amount of cold-welding that is apparent in these samples, the small amount of Ti remaining must be sufficient to accommodate the formation of the large flakes seen in the high Ti-content samples, but it is present in insufficient quantity to cause significant cold welding in the Ti-poor $\text{Si}_{85}\text{Ti}_{15}$ (N_2) alloy.

After longer milling durations (90 min in the case of the $\text{Si}_{70}\text{Ti}_{30}$ (N_2) alloy and 960 min in the case of the $\text{Si}_{60}\text{Ti}_{40}$ (N_2) alloy), the flakes disappear. After 960 min of milling all samples consist of irregularly shaped submicron particles and their aggregates. The alloys have apparently become completely brittle and unable to cold-weld. According to the XRD patterns shown in Fig. 2, these samples consist mainly of α -Si and TiN phases with some trace Ti or Fe impurity in some cases. Only at this stage in the milling process has the ball milling reaction between Si, Ti, and N completed and only at this stage has all of the α -Si phase been converted to α -Si.

Changes in sample morphology during the milling process were quantified by measuring the specific surface area of each sample, shown in Fig. S2. Because of the different compositions of each series of samples and their changing compositions during the milling process, to better compare surface areas these values were converted

to volumetric surface area (VSA) values utilizing true density values as measured by He-pycnometry. Measured surface areas and densities are listed in Table S1. Figure 4 shows the VSA of the $\text{Si}_{85}\text{Ti}_{15}$ (N_2), $\text{Si}_{70}\text{Ti}_{30}$ (N_2), and $\text{Si}_{60}\text{Ti}_{40}$ (N_2) alloys during the ball milling process. For all samples, the VSA reduces with milling time and then reaches a minimum surface area after 60–75 min of milling time. Extended milling results in an increase in VSA. The $\text{Si}_{85}\text{Ti}_{15}$ (N_2) sample has the highest VSA at all milling times. After 30 min milling, the VSA is nearly $60 \text{ m}^2 \text{ ml}^{-1}$. This high value is presumably due to the large amount of brittle Si and low amount of ductile Ti in this sample. However, increased milling time still results in a significant ($\sim 37\%$) decrease in surface area to a minimum VSA value of $38 \text{ m}^2 \text{ ml}^{-1}$, indicating that some cold welding still takes place in this sample. Extending the milling time results in the VSA to increase to $48 \text{ m}^2 \text{ ml}^{-1}$, as the ductile Ti phase is replaced by brittle TiN. The VSA of the higher Ti containing $\text{Si}_{70}\text{Ti}_{30}$ (N_2), and $\text{Si}_{60}\text{Ti}_{40}$ (N_2) alloys are much lower than that of $\text{Si}_{85}\text{Ti}_{15}$ (N_2). After only 30 min milling the VSA of these alloys is already below $30 \text{ m}^2 \text{ ml}^{-1}$. The lowest VSA of only $10 \text{ m}^2 \text{ ml}^{-1}$ is achieved by $\text{Si}_{60}\text{Ti}_{40}$ (N_2), the highest Ti-containing alloy after 60 min of milling. As with $\text{Si}_{85}\text{Ti}_{15}$ (N_2), extending the milling time further causes the VSA to increase, with $\text{Si}_{60}\text{Ti}_{40}$ (N_2) again being achieving the lowest VSA of $30 \text{ m}^2 \text{ ml}^{-1}$. However, this is only

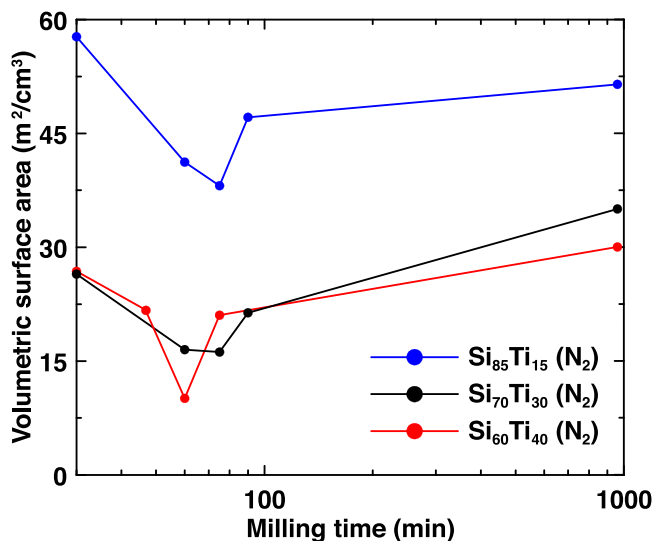


Figure 4. Volumetric surface area during milling of $\text{Si}_x\text{Ti}_{100-x}$ ($x = 85, 70,$ and $60, \text{N}_2$) samples.

slightly lower than the $\text{Si}_{70}\text{Ti}_{30}(\text{N}_2)$ alloy. These observations are consistent with the trends described above in the SEM images of Fig. 3.

The trends in alloy grain size, reaction extent, particle size, and surface area shown in Figs. 2–4 all roughly follow the same trends as shown in Fig. 1. These trends can be summarized as follows.

0–~75 min milling time:

1. cold welding of Ti phase
2. x -Si phase converts to α -Si phase
3. particle size increases, VSA decreases
4. $2\text{Si}(\text{s}) + \text{Ti}(\text{s}) \rightarrow \text{TiSi}_2(\text{s})$ reaction decreases amount of Ti phase in samples

~75 min milling time:

1. $2\text{Si}(\text{s}) + \text{Ti}(\text{s}) \rightarrow \text{TiSi}_2(\text{s})$ has depleted the Ti phase in the samples
2. fracturing processes start to dominate cold welding
3. maximum particle size and minimum VSA achieved >75 min milling time:
4. fractured TiSi_2 phase becomes susceptible to reaction with N_2
5. $\text{TiSi}_2(\text{s}) + \text{N}_2(\text{g}) \rightarrow 2\text{TiN}(\text{s}) + 4\text{Si}(\text{s})$ reaction proceeds
6. particle size decreases, VSA increases

The above analysis sheds light on why the ball milling reaction between Si, Ti and $\text{N}_2(\text{g})$ occurs in the two consecutive stages described by Eqs. 1a and 1b. During the initial milling steps Si, Ti, and TiSi_2 phases are all available for reaction with $\text{N}_2(\text{g})$. We have observed that Si on its own does not react with $\text{N}_2(\text{g})$ under the ball milling conditions used here. Although such a reaction would be thermodynamically favorable, the activation barrier for breaking the N_2 triple bond may be too great for this reaction to proceed. Thermodynamically, Ti, and TiSi_2 also should react with $\text{N}_2(\text{g})$, however, during the initial stages of ball milling, as shown in Figs. 3 and 4, cold welding and the lack of particle fracturing because of the presence of the ductile Ti phase essentially inhibits any reaction with the $\text{N}_2(\text{g})$ atmosphere in the mill. Only after all of the Ti phase is consumed by reacting with Si according to Eq. 1a, does fracture begin to dominate. At this point, the only reactive phase present is TiSi_2 . Fracture of this phase exposes fresh surfaces that may react with $\text{N}_2(\text{g})$, resulting in the formation of TiN, according to Eq. 1b.

As mentioned in the introduction, the situation shown in Fig. 1 or 4, presents a dilemma in the synthesis of practical Si–Ti–N alloy. Although minimum surface areas are desirable, at the milling time in which the minimum VSA is reached in Fig. 4, the alloys still contain considerable x -Si phase and the milling reaction has not gone to completion. In order to create a fully nanostructured Si–Ti–N alloy with low surface area, the above results suggested to us that a 2-step preparation method might be utilized, according to the illustration shown in Fig. S3. In the first step, Si and Ti powders were milled in

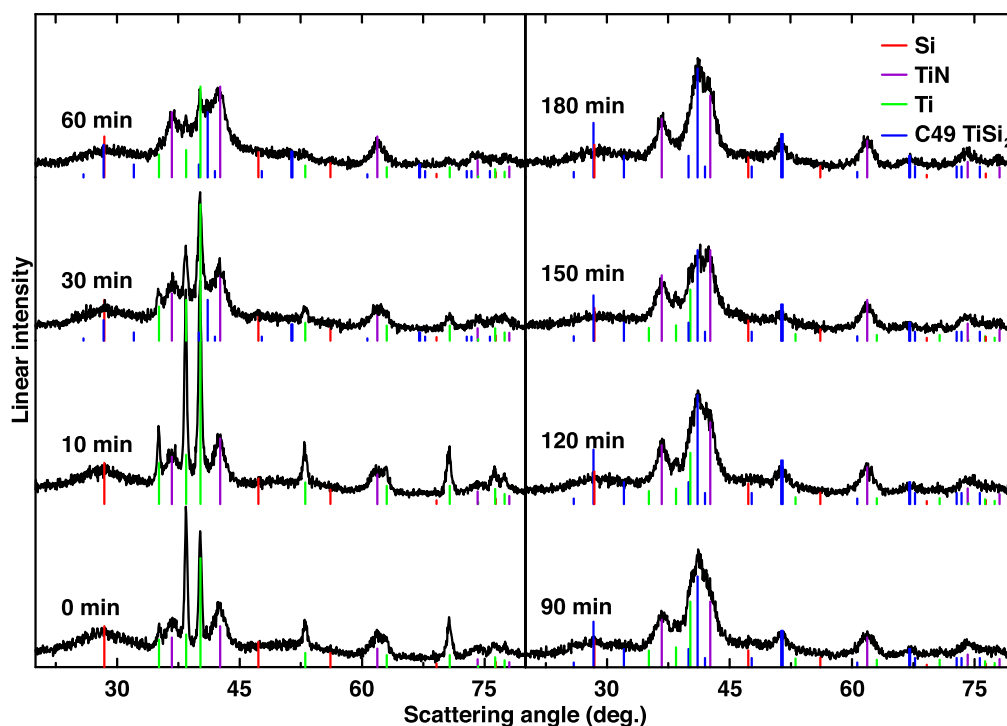


Figure 5. XRD patterns of $\text{Si}_{62.5}\text{Ti}_{26.8}\text{N}_{10.7}$ alloys prepared using the 2-step milling procedure described in the manuscript. Second step milling times are indicated.

N₂ (g) for 16 h, to give a Si₈₅(TiN)₁₅ alloy. According to Fig. 2a, this alloy consists of nanocrystalline TiN (Scherrer gain size: 5 nm) and a-Si. This nanostructure is ideal for a Si-based anode. However, as shown in Fig. 4, the surface area of this alloy is high. In order to reduce the surface area, the pre-milled alloy was then ball milled with additional Ti powder, to result in a final alloy composition of Si_{62.5}Ti_{26.8}N_{10.7} (corresponding to a 70:30 Si:Ti ratio) and ball milling was continued under Ar gas. As illustrated in Fig. S3, the ductile Ti is expected to cold-weld the pre-milled alloy particles together and simultaneously react with Si to form TiSi₂. Additionally, since all of the Si phase has been previously amorphized in the first milling step (Step 1 in Fig. S3), it should remain fully amorphous throughout the second milling step (Step 2 in Fig. S3) of the reaction. If ball milling is stopped when all of the Ti phase is consumed (as indicated in Fig. S3), then this should result in a fully nanostructured a-Si + TiN + TiSi₂ alloy with low surface area. Based on the total amounts of precursor powders added to the mill, the final phase composition should be 30.3a-Si + 16.1TiSi₂ + 10.7TiN, which has a theoretical capacity of 955 mAh g⁻¹, based on the a-Si phase forming Li_{3.75}Si after full lithiation.

Figure 5 shows XRD patterns of Si_{62.5}Ti_{26.8}N_{10.7} alloys prepared using the above 2-step milling procedure, with different 2nd step milling times as indicated. As shown in the XRD pattern of the alloy with a 2nd milling time of 0 min, the first milling step resulted in an alloy with a completely amorphous Si phase and a nanocrystalline TiN phase. Sharp peaks in this XRD pattern correspond to unmilled Ti powder that was added to the alloy after the first milling step. As expected, for alloys with longer second milling step times the Si phase remained completely amorphous. The nanocrystalline TiN phase present was also unaffected by the 2nd milling step. Also as expected, the added Ti was consumed continuously during the 2nd milling step in Ar by reacting with Si to produce C49 TiSi₂. After about 90 min the Ti phase was nearly completely consumed and the phases remaining are a-Si + TiN + TiSi₂. Near this milling time, a minimum in the alloy surface area is expected, according to the above results.

Figure S4 shows TEM images of the alloy after 120 min of milling in the second step. It is composed of ~10 nm nanoparticles dispersed in an amorphous matrix. Figure S5 shows an electron diffraction pattern of the alloy. A list of the observed diffraction rings, d-spacings and identified corresponding phases is provided in Table SII. The most intense diffraction rings correspond well with the d-spacings and intensities expected from TiN. Diffraction rings were also observed that were consistent with the most intense reflections of C49 TiSi₂. The most intense reflection of Ti is coincident with d-spacings from TiN and TiSi₂. Therefore, the presence of some nanocrystalline Ti could not be ruled out in this sample. No diffraction rings corresponding to the d-spacings of Si were observed. This is consistent with the observed low electron density matrix phase being amorphous Si. In summary, XRD and TEM results show that after ~90 min of milling in the second step, these alloys consist of nanocrystalline TiN and C49-TiSi₂ particles, and possibly some Ti particles, about 10 nm in size dispersed in an amorphous Si matrix.

Figure 6 shows SEM images of 2-step Si_{62.5}Ti_{26.8}N_{10.7} alloys with different 2nd step milling times. The Si_{62.5}Ti_{26.8}N_{10.7} 2-step sample (0 min) is a mixture of small Si-TiN particles prepared in the initial milling step and big Ti-rich flakes (dozens of micrometers). These Ti flakes represent the added Ti powder after the 2nd step which have been exposed to milling in ethanol for sample collection. As the 2nd step milling time is increased from 10–120 min, the alloy particle size becomes larger. As with the 1-step alloys, flake-like particles begin to form, with the largest flakes (~1 μm × 2–5 μm) forming after 120 min of 2nd step milling. This is near to the time observed by XRD when the Ti-phase has disappeared, as expected. With increasing milling time, the particles become smaller, as insufficient Ti-phase is present to support cold-welding and particle fracturing becomes the dominant process.

The VSA of the 2-step Si_{62.5}Ti_{26.8}N_{10.7} alloys as a function of 2nd step milling time is shown in Fig. 7 (specific surface areas are shown in Fig. S6). Also shown are the VSAs of a Si₈₅Ti₁₅ (N₂, 960 min) single-step sample (i.e. the alloy to which Ti was added to make the 2-step Si_{62.5}Ti_{26.8}N_{10.7} alloys) and a Si₇₀Ti₃₀ (N₂, 960 min) single-step sample (an 1-step alloy having the same 70:30 Si:Ti ratio as the 2-step Si_{62.5}Ti_{26.8}N_{10.7} alloys). The trend in the VSA of the 2-step Si_{62.5}Ti_{26.8}N_{10.7} alloys with time is consistent with the trends in particle size shown in Fig. 6. A minimum VSA of 23.5 m² ml⁻¹ was attained after 120 min 2nd-step milling. This represents nearly a 60% reduction in VSA during the 2nd milling step process, a 48% reduction in VSA compared to Si₇₀Ti₃₀ (N₂, 960 min) and a 104% reduction in VSA compared to Si₈₅Ti₁₅ (N₂, 960 min). According to the XRD patterns shown in Fig. 5, the Si_{62.5}Ti_{26.8}N_{10.7} alloy after 120 min 2nd-step milling, corresponding to the sample with the minimum VSA, is fully nanostructured with a completely amorphous active Si phase. Therefore, utilizing the 2-step milling procedure significant reductions in VSA were attained while achieving a fully nanostructured alloy.

Figure 8a shows the first four cycles of potential (vs Li)-capacity profiles of 2-step Si_{62.5}Ti_{26.8}N_{10.7} alloys prepared with different 2nd step milling times. All these Si alloys display a pair of sloping plateaus during lithiation/delithiation, which are characteristic of the lithiation/delithiation of a-Si without Li₁₅Si₄ formation.¹⁶ The reversible capacities and initial coulombic efficiencies of the 2-step Si_{62.5}Ti_{26.8}N_{10.7} alloy cells are listed in Table I. As the 2nd milling step time is increased, more active Si reacts with the added Ti, resulting in a decrease in reversible capacity. This also has an effect of reducing their ICEs. Differential capacity curves of the 2-step Si_{62.5}Ti_{26.8}N_{10.7} alloys prepared with different 2nd step milling times are shown in Fig. 8b for different cycles, as indicated. During the first lithiation, all samples show a peak at around 0.25 V–0.35 V corresponding to the nucleation and growth of lithiated Si. Subsequently, all differential capacity curves show 2 broad lithiation and 2-broad delithiation peaks corresponding to the lithiation and delithiation of a-Li_xSi. However, by the 35th cycle, the 60 min 2nd-step Si_{62.5}Ti_{26.8}N_{10.7} alloy is beginning to show early signs of Li₁₅Si₄ formation, with a very broad Li₁₅Si₄ delithiation peak apparent at about 0.45 V.¹⁷ The formation of Li₁₅Si₄ is thought to be detrimental for Si-based anode materials, as it could result in active Si disconnection from a supporting matrix and internal fracturing of alloy particles.¹⁸

Figure 9a shows the specific discharge capacity and Fig. 9b the CEs of the 2-step Si_{62.5}Ti_{26.8}N_{10.7} alloys prepared with different 2nd step milling times. The 60 min 2-step sample shows a larger fade rate after cycle 60, possibly because of the formation of Li₁₅Si₄ during cycling in in this sample, as discussed above. All of the other samples have similar fade rates over the 100 tested cycles. This indicates that the surface area of the synthesized alloy does not greatly impact the fade rate in the 100 cycles shown. Indeed, Ref. 5 reports a Si₆₀(TiN)₄₀ alloy prepared by conventional single-step milling in N₂ consisting of submicron particles, its capacity and fade rate being nearly identical to that of the 120 min 2-step sample consisting of ~3 μm particles. This further confirms that the larger flake morphologies have little impact on the cycling performance of this alloy. The 120 min 2nd step sample has a reversible capacity of 900 mAh g⁻¹, which corresponds to a volumetric capacity of 1529 Ah l⁻¹ at full volume expansion (according to the method of calculating volumetric alloy capacities described in Ref. 19). As shown in Fig. 9b, all the 2-step Si_{62.5}Ti_{26.8}N_{10.7} alloys show no obvious differences in their CEs, despite large differences in the surface areas of these alloys.

BSE images of cross sections of the 2-step Si_{62.5}Ti_{26.8}N_{10.7} alloy electrodes after 100 charge/discharge cycles are shown in Fig. 10. Bright areas in the image correspond to the alloy phase, whereas grey areas correspond to either porosity or eroded alloy combined with SEI products.^{5,20} All of the cycled Si alloys show surface erosion during cycling, which means an increase of surface area. It is suspected that this erosion is the cause of the linear fade observed in

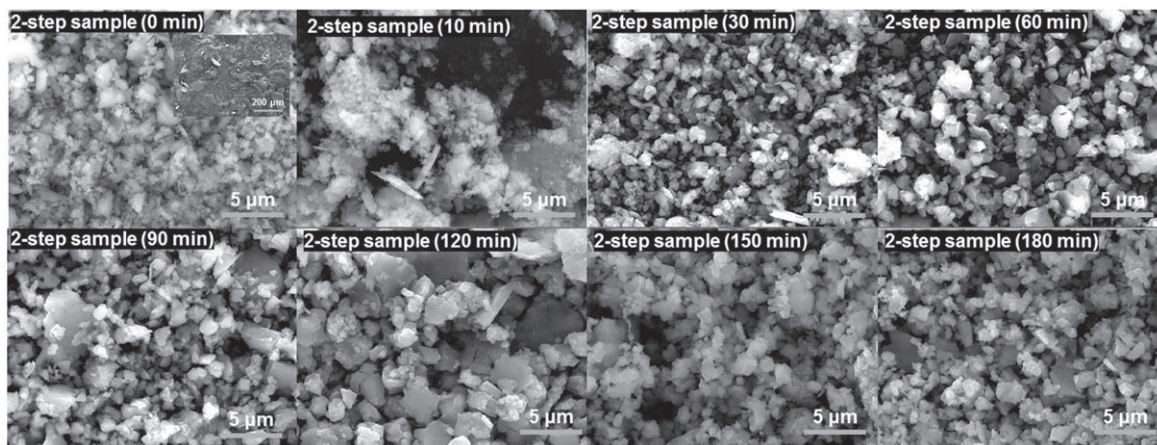


Figure 6. SEM SE images of $\text{Si}_{62.5}\text{Ti}_{26.8}\text{N}_{10.7}$ alloys prepared using the 2-step milling procedure described in the manuscript. Second step milling times are indicated.

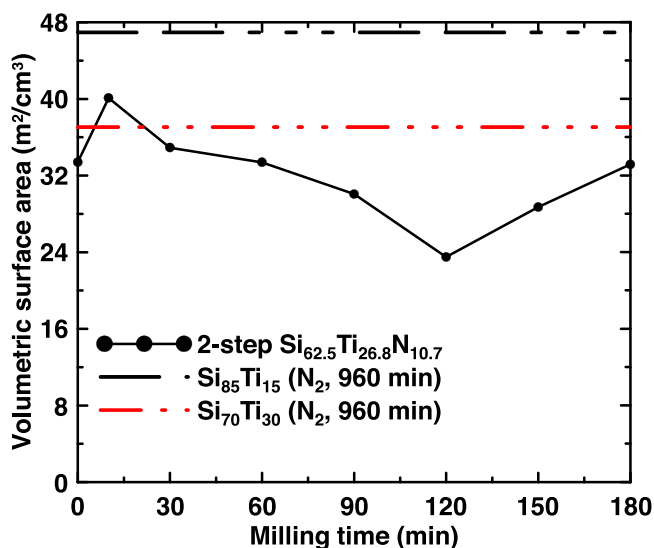


Figure 7. Volumetric surface area of $\text{Si}_{62.5}\text{Ti}_{26.8}\text{N}_{10.7}$ alloys prepared using the 2-step milling procedure described in the manuscript. Second step milling times are indicated. VSAs of a $\text{Si}_{85}\text{Ti}_{15}$ (N_2 , 960 min) single-step sample (i.e. the alloy to which Ti was added to make the 2-step $\text{Si}_{62.5}\text{Ti}_{26.8}\text{N}_{10.7}$ alloys) and a $\text{Si}_{70}\text{Ti}_{30}$ (N_2 , 960 min) single-step sample (an 1-step alloy having the same 70:30 Si:Ti ratio as the 2-step $\text{Si}_{62.5}\text{Ti}_{26.8}\text{N}_{10.7}$ alloys) are shown for comparison.

Fig. 9. No significant differences can be seen in the extent of the erosion of the alloy surfaces for the different alloys shown in Fig. 10. Similarly, there is no significant difference in the fade rate between the 2-step samples. Therefore, reducing the surface area of these alloys may not have resulted in any significant reduction in surface reactivity. The highly fractured surface of the alloy that forms during cycling likely results in a high reactivity with electrolyte, regardless

of what the surface area of the alloy was initially. Therefore, alloy surface area reduction may not be a good strategy to reduce surface reactivity. This is a surprising result that requires confirmation with other alloy systems.

In order to show the 2-step preparation method can be applied to other alloy compositions, $\text{SiO}_{0.37}$ was prepared by ball milling Si in air, as described in Ref. 21. An XRD pattern and SEM image of this sample are shown in Figs. S7 and S8, respectively. $\text{SiO}_{0.37}$ is fully amorphous. It consists of irregularly-shaped fine submicron particles, leading to a large $63.2 \text{ m}^2 \text{ ml}^{-1}$ VSA. To reduce the surface area of this sample, Ti powder was added to result in a final sample composition of $\text{Si}_{63.0}\text{O}_{23.3}\text{Ti}_{13.7}$ and a 2nd milling step was conducted in $\text{Ar}(\text{g})$ for 180 min. The VSA of the 2-step $\text{Si}_{63.0}\text{O}_{23.3}\text{Ti}_{13.7}$ alloy was measured to be $41.5 \text{ m}^2 \text{ ml}^{-1}$, representing a significant 34% reduction compared to the 1-step $\text{Si}_{73.0}\text{O}_{27.0}$ alloy. Figure S7 shows the XRD pattern of the 2-step $\text{Si}_{63.0}\text{O}_{23.3}\text{Ti}_{13.7}$ alloy. The additional Ti has reacted during the 2nd milling step to form TiSi_2 . However, a significant amount of Ti remains. Therefore, it is suspected that further milling might result in a lower VSA than achieved here. An SEM image of the 2-step $\text{Si}_{63.0}\text{O}_{23.3}\text{Ti}_{13.7}$ alloy is shown in Fig. S8. It contains much larger particles ($4 \mu\text{m} - 8 \mu\text{m}$) compared to the submicron particles of the starting $\text{SiO}_{0.37}$ alloy, but many submicron particles remain. This demonstrates that the 2-step milling method can also be used to realize significant surface area reductions in other alloy chemistries. In this system careful study is needed to determine optimal amounts of oxygen, active Si and Ti to achieve minimal surface area while maintaining high volumetric capacity. We are currently investigating the use of this method to produce this and other low surface area alloy compositions and particularly the effect of metals other than Ti as ductile additives for surface area reduction during the second milling step.

Conclusions

The surface area evolution of Si–Ti–N alloys were studied by ball milling Si and Ti powders in N_2 (g) for different times. Low surface areas ($\sim 15 \text{ m}^2 \text{ ml}^{-1}$) can be obtained after short milling times

Table I. ICE, reversible capacity, and 100th-cycle capacity retention of Si-Ti-N 2-step samples (60–180 min).

Sample	ICE (%)	Reversible capacity (mAh g^{-1})	100th-cycle capacity retention (%)
2-step sample (60 min)	87.1 ± 0.2	1231.3 ± 3.6	77.6 ± 0.5
2-step sample (90 min)	85.1 ± 0.1	1044.0 ± 21.0	80.3 ± 1.3
2-step sample (120 min)	82.9 ± 1.1	926.4 ± 31.5	82.8 ± 0.4
2-step sample (150 min)	77.4 ± 0.1	882.1 ± 12.3	81.2 ± 0.7
2-step sample (180 min)	81.1 ± 0.1	920.9 ± 8.7	82.9 ± 0.9

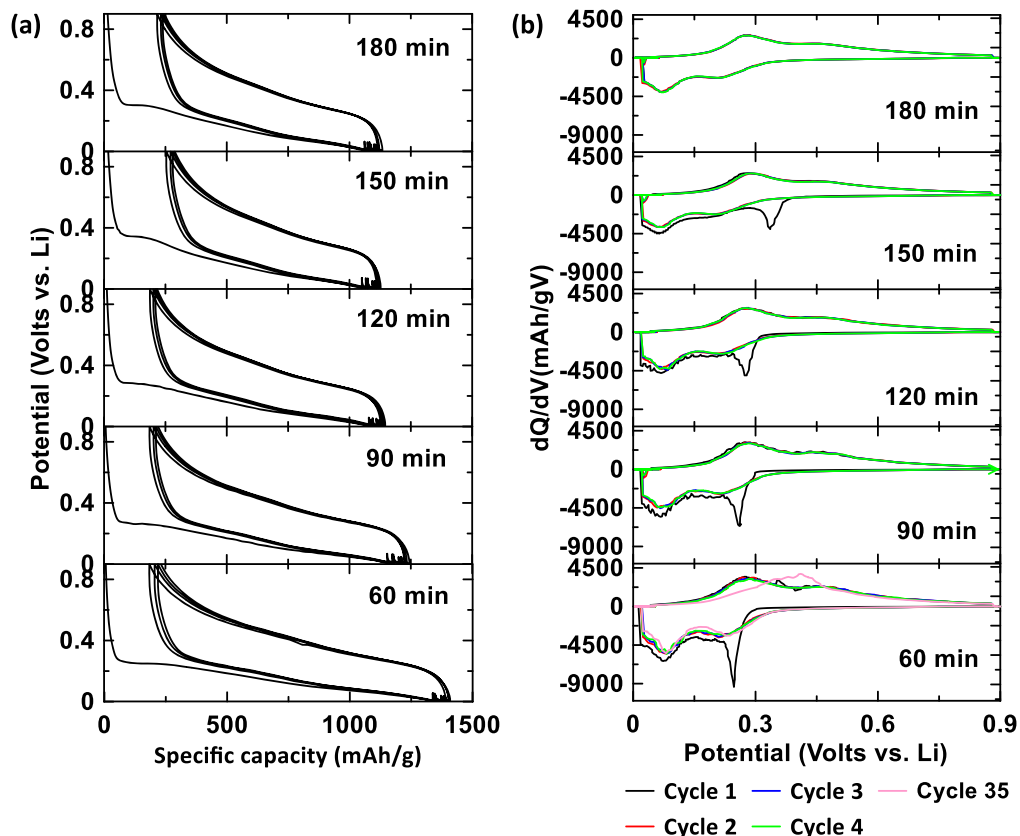


Figure 8. (a) The first four cycles of potential (vs Li)-capacity profiles and (b) differential capacity (dQ/dV)-potential (vs Li) curves of $\text{Si}_{62.5}\text{Ti}_{26.8}\text{N}_{10.7}$ alloys prepared using the 2-step milling procedure described in the manuscript. Second step milling times are indicated.

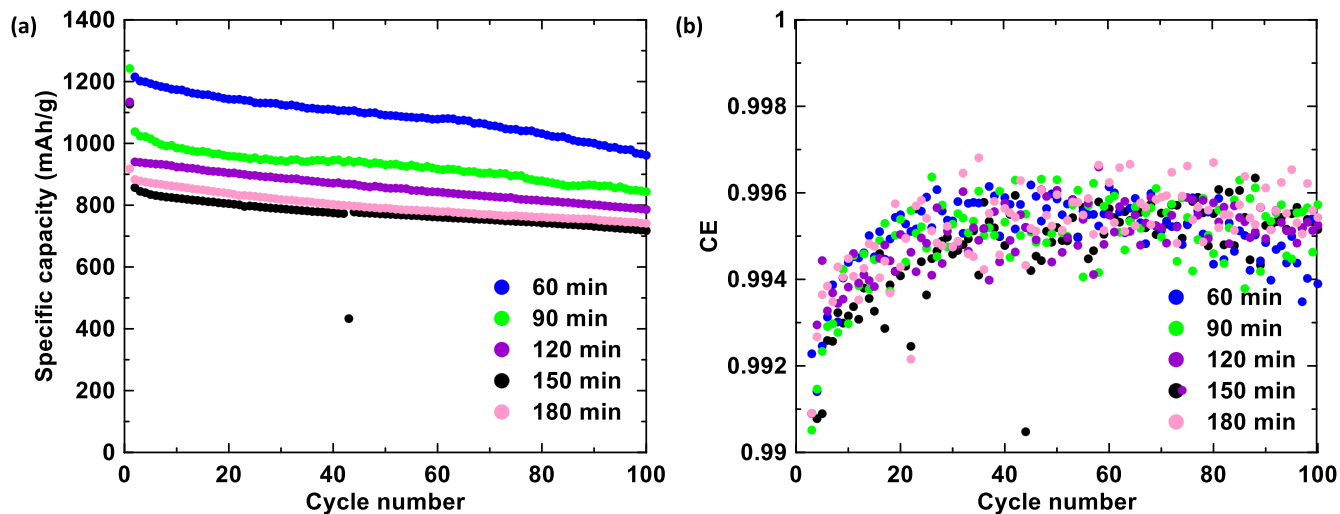


Figure 9. (a) specific discharge capacity and (b) CE of $\text{Si}_{62.5}\text{Ti}_{26.8}\text{N}_{10.7}$ alloys prepared using the 2-step milling procedure described in the manuscript. Second step milling times are indicated.

(~75 min), however this is not sufficient time for the precursors to fully react or for a fully amorphous active Si phase to be formed. Further milling results in particle size reduction and increased surface area. To achieve fully reacted low surface area Si-Ti-N alloys with an amorphous Si active phase, a 2-step milling method was developed. In the first milling step, a long milling time (16 h) was applied for obtaining fully reacted Si-Ti-N alloys with an amorphous Si active phase. In the second milling step, additional Ti is added, and the alloy is milled further in Ar (10 to 180 min) to achieve low surface areas.

This second milling step resulted in a 104% reduction in volumetric surface area. The second step also made the alloy more Ti-rich. Compared to an alloy prepared conventionally with the same final Si: Ti ratio, the 2-step process still resulted in a substantial surface area reduction of 30%. The same method was used to lower the surface area of SiO_2 , by adding Ti in a second milling step, resulting in a Si-Ti-O alloy with 34% less volumetric surface area. We believe the 2-step milling method developed here is a simple and inexpensive method to obtain Si-metal alloys with low surface area. However,

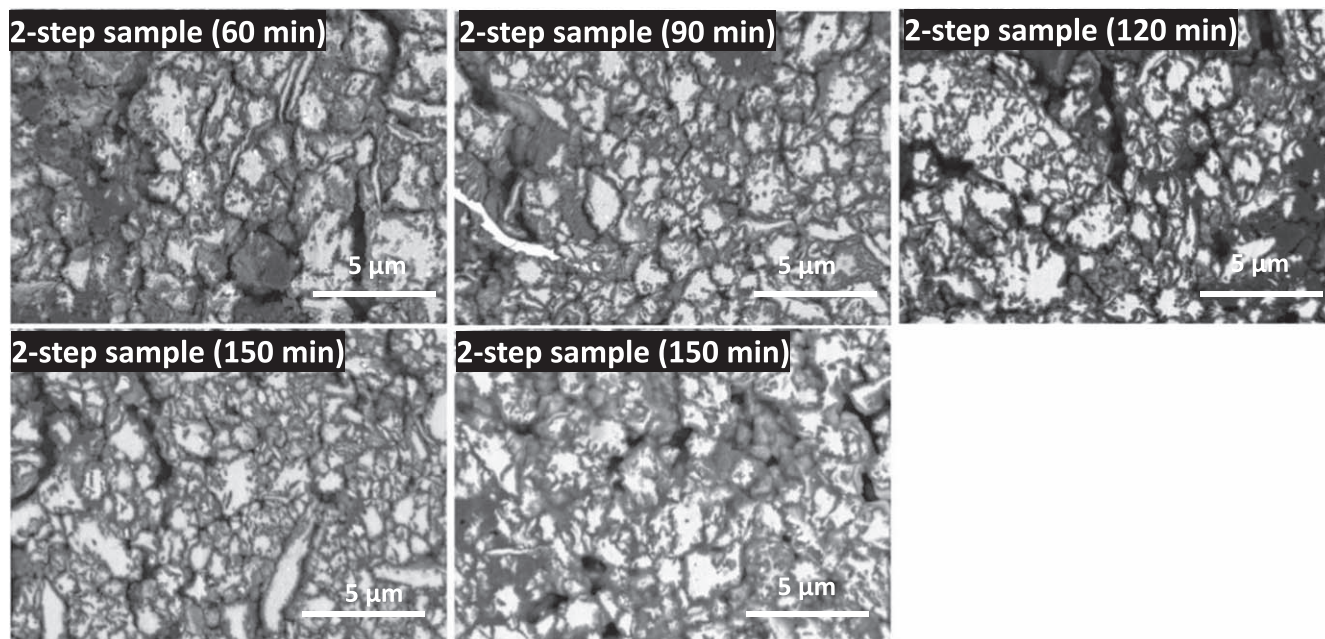


Figure 10. SEM BSE images of electrode cross sections of $\text{Si}_{62.5}\text{Ti}_{26.8}\text{N}_{10.7}$ alloys prepared using the 2-step milling procedure described in the manuscript. Second step milling times are indicated.

significant reductions in surface area, did not result in any obvious electrochemical performance difference compared to conventionally ball milled high surface area alloy materials. This is likely because cycling caused severe fracturing of the alloy surfaces, resulting in a high surface area, regardless of the initial surface area of the alloy. This suggests that, unlike other anode materials such as graphite, the initial surface area of Si alloys does not translate into reduced electrolyte reactivity.

Acknowledgments

The authors acknowledge financial support from NSERC, NOVONIX Battery Technology Solutions, the Canada Foundation for Innovation, and the Atlantic Innovation Fund for this work. Simeng Cao would like to acknowledge Dr Xiang Yang for his kind assistance in operating SEM.

ORCID

Mohammad H. Tahmasebi  <https://orcid.org/0000-0003-1907-5806>

M. N. Obrovac  <https://orcid.org/0000-0001-5509-3185>

References

- M. D. Fleischauer, M. N. Obrovac, and J. R. Dahn, "Simple model for the capacity of amorphous silicon-aluminum-transition metal negative electrode materials." *J. Electrochem. Soc.*, **153**, A1201 (2006).
- M. D. Fleischauer, J. M. Topple, and J. R. Dahn, "Combinatorial investigations of Si-M (M = Cr + Ni, Fe, Mn) thin film negative electrode materials." *Electrochem. Solid-State Lett.*, **8**, A137 (2005).
- X. Zhao, R. J. Sanderson, M. A. Al-Maghrabi, R. A. Dunlap, and M. N. Obrovac, "Electrochemistry of sputtered and ball milled Si-Fe-O alloys in Li cells." *J. Electrochem. Soc.*, **164**, A1165 (2017).
- M. T. McDowell, S. W. Lee, J. T. Harris, B. A. Korgel, C. Wang, W. D. Nix, and Y. Cui, "In situ TEM of two-phase lithiation of amorphous silicon nanospheres." *Nano Lett.*, **13**, 758 (2013).
- S. Cao, J. C. Bennett, Y. Wang, S. Gracious, M. Zhu, and M. N. Obrovac, "Si-TiN alloy Li-ion battery anode materials prepared by reactive N_2 Gas milling." *J. Power Sources*, **438**, 2270003 (2019).
- Y. Wang, S. Cao, H. Liu, M. Zhu, and M. N. Obrovac, "Si-TiN alloy li-ion battery negative electrode materials made by N_2 Gas milling." *MRS Commun.*, **8**, 1352 (2018).
- S. Cao, M. H. Tahmasebi, J. C. Bennett, and M. N. Obrovac, "Si-TiN alloy anode materials prepared by reactive N_2 gas milling: thermal stability and electrochemistry in Li-cells." *Electrochim. Acta*, **396**, 139259 (2021).
- K. Schroder, J. Alvarado, T. A. Yersak, J. Li, N. Dudney, L. J. Webb, Y. S. Meng, and K. J. Stevenson, *Chem. Mater.*, **27**, 5531 (2015).
- H. Nakai, T. Kubota, A. Kita, and A. Kawashima, "The effect of fluoroethylene carbonate as an additive on the solid electrolyte interphase on silicon lithium-ion electrodes." *J. Electrochem. Soc.*, **158**, A798 (2011).
- H. Wu and Y. Cui, "Designing nanostructured Si anodes for high energy lithium ion batteries." *Nano Today*, **7**, 414 (2012).
- P. Y. Lee, J. L. Yang, and H. M. Lin, "Amorphization behaviour in mechanically alloyed Ni-Ta powders." *Journal Mater. Sci.*, **33**, 235 (1998).
- C. Suryanarayana, "Mechanical alloying and milling." *Prog. Mater. Sci.*, **46**, 1 (2001).
- M. N. Obrovac and V. L. Chevrier, "Alloy negative electrodes for li-ion batteries." *Chem. Rev.*, **114**, 11444 (2014).
- Y. Wang, S. Cao, M. Kalinia, L. Zheng, L. Li, M. Zhu, and M. N. Obrovac, "Lithium insertion in nanostructured $\text{Si}_{1-x}\text{Ti}_x$ alloys." *J. Electrochem. Soc.*, **164**, A3006 (2017).
- T. D. Hatchard, A. Genkin, and M. N. Obrovac, "Rapid mechanochemical synthesis of amorphous alloys." *AIP Adv.*, **7**, 045201 (2017).
- Z. Du, T. D. Hatchard, R. A. Dunlap, and M. N. Obrovac, "Combinatorial investigations of Ni-Si negative electrode materials for Li-Ion batteries." *J. Electrochem. Soc.*, **162**, A1858 (2015).
- M. N. Obrovac and L. Christensen, "Structural changes in silicon anodes during lithium insertion/extraction." *Electrochem. Solid-State Lett.*, **7**, A93 (2004).
- D. S. M. Iaboni and M. N. Obrovac, " $\text{Li}_{15}\text{Si}_4$ formation in silicon thin film negative electrodes." *Electrochem. Soc.*, **163**, A255 (2016).
- M. N. Obrovac, L. Christensen, D. Ba Le, and J. R. Dahn, "Alloy design for lithium-ion battery anodes." *J. Electrochem. Soc.*, **154**, A849 (2007).
- L. J. Krause, T. Brandt, V. L. Chevrier, and L. D. Jensen, "Surface area increase of silicon alloys in Li-Ion full cells measured by isothermal heat flow calorimetry." *J. Electrochem. Soc.*, **164**, A2277 (2017).
- Y. Cao, J. C. Bennett, R. A. Dunlap, and M. N. Obrovac, "A simple synthesis route for high-capacity SiOx anode materials with tunable oxygen content for lithium-ion batteries." *Chem. Mater.*, **30**, 7418 (2018).